01 Dec 2020

Bond Behavior between Steel Fiber Reinforced Polymer (SRP) and Concrete

Xingxing Zou

Lesley Sneed
Missouri University of Science and Technology, sneedlh@mst.edu

Follow this and additional works at: https://scholarsmine.mst.edu/civarc_enveng_facwork

Part of the Structural Engineering Commons

Recommended Citation

International Journal of Concrete
Structures and Materials

RESEARCH   **Open Access**

Bond Behavior Between Steel Fiber Reinforced Polymer (SRP) and Concrete

Xingxing Zou and Lesley H. Sneed[*]

Abstract

Steel fiber reinforced polymer (SRP) composite materials, which consist of continuous unidirectional steel wires (cords) embedded in a polymeric matrix, have recently emerged as an effective solution for strengthening of reinforced concrete (RC) structures. SRP is bonded to the surface of RC structures by the same matrix to provide external reinforcement. Interfacial debonding between the SRP and concrete is a primary concern in this type of application. This study aimed to investigate the bond characteristics between SRP and concrete determined by single-lap direct shear tests with different composite bonded lengths and fiber sheet densities (cord spacings). Specimens with medium density fibers failed mainly due to composite debonding, whereas those with low density fibers failed due to fiber rupture. Results of specimens that exhibited debonding were used to determine the bond-slip relationship of the SRP-concrete interface and to predict the full-range load response, which was in good agreement with the experimental results. A database of SRP-concrete direct shear tests reported in the literature was also established. Four analytical equations derived for fiber reinforced polymer (FRP)-concrete debonding were evaluated based on the database results and were found to predict the maximum load within approximately 15% error on average, however, they all underestimated the effective bond length.

Keywords: effective bond length, fiber reinforced polymer (FRP), interfacial debonding, single-lap direct shear test, steel fiber reinforced polymer (SRP)

1 Introduction

The increasing use of fiber reinforced polymer (FRP) composites for strengthening and repairing existing reinforced concrete (RC) structures has prompted an extensive research effort in the last three decades (Triantafillou and Deskovic 1991; Bakis et al. 2002). Experimental and analytical research has shown that externally bonded (EB) FRP can provide substantial increases in flexural (Chen et al. 2018; Attari et al. 2012; Pan and Leung 2007), shear (Khalifa and Nanni 2000), and torsional (Hii and Al-Mahaidi 2007; Alabdulhady and Sneed 2019) strength and deformability to RC structures. Since 2004, a new type of composite material comprised of high strength

steel fiber cords and a polymeric matrix has been explored for the use of strengthening and repairing RC structures (Wobbe et al. 2004). Steel fiber reinforced polymer composite is referred to as SRP composite in this paper. High strength steel fibers are produced in the form of steel wires twisted into cords. Typically a zinc or brass coating is provided to protect the steel cords against corrosion (Wobbe et al. 2004; Ascione et al. 2017; Górski et al. 2013; Prota et al. 2004). The use of steel cords results in certain advantages over other fiber types used in traditional FRP composites (e.g., carbon, glass) including relatively high stiffness, high ductility, and low vulnerability to rupture when bent or wrapped around cross sections with sharp corners (Ascione et al. 2017; Górski et al. 2013; Prota et al. 2004; Figeys et al. 2008). Additionally, the higher strength perpendicular to the steel fiber axial direction can enable more effective gripping and anchoring in prestressed applications (Górski et al.

*Correspondence: sneedlh@mst.edu
Department of Civil, Architectural and Environmental Engineering, Missouri University of Science and Technology, Rolla, MO, USA

2013). Flexural tests of RC beams strengthened with EB SRP have demonstrated the efficacy of SRP in improving the flexural strength and ductility of RC beams (Wobbe et al. 2004; Prota et al. 2004; Figeys et al. 2005; Pecce et al. 2006). These encouraging experimental results have prompted producers and researchers to develop commercially available products, useful laboratory data, analytical design methods, and field applications for SRP composites (Ascione et al. 2017; Kerakoll 2020; Matana et al. 2005).

Interfacial debonding of the composite has been proven to be one of the most important causes of structural failure of RC members strengthened with EB FRP composites (Attari et al. 2012; Khalifa and Nanni 2000; Hii and Al-Mahaidi 2007). Therefore, much attention has been paid to the debonding mechanism in RC structures strengthened with EB FRP composites. It is well-understood that debonding of FRP composites typically occurs at the composite-concrete interface with fracture occurring within a thin layer of concrete directly beneath the composite (ACI 440.2R-17 2017). Likewise, many of the experimental studies on RC beams strengthened with EB SRP reported failure due to composite debonding, which occurred within a thin layer of concrete substrate beneath the composite (Górski et al. 2013; Prota et al. 2004; Figeys et al. 2008; Figeys et al. 2005). Several studies have been conducted to study the SRP-concrete debonding phenomenon (Ascione et al. 2017; Matana et al. 2005; Mitolidis et al. 2008; Carloni et al. 2017), although methods to predict the bond behavior are still under development. Since there has been a large number of experimental, analytical, and numerical studies on FRP-concrete debonding (Mukhtar and Faysal 2018; Wu and Jiang 2013; Zhang et al. 2018), a question faced by researchers is whether existing design methods for FRP can be used for SRP in an analogous way.

The mechanical characteristics of SRP are different from those of FRP in terms of strength, stiffness, and ductility. Pure tension tests of SRP plates showed that the stress−strain behavior is nonlinear, which is different from the elastic behavior until failure of traditional FRP (Matana et al. 2005; Carloni et al. 2017; Kim et al. 2005; Santandrea 2018). Moreover, the study in (Figeys et al. 2008) showed that SRP is stiffer and stronger than CFRP, and the existing equations to predict the minimum length required to fully develop the stress transfer zone (STZ) (i.e., the effective bond length, L_e) and the load causing interfacial debonding when the STZ is fully established (P_{deb}) for FRP-concrete joints should be adjusted for SRP. Therefore, efforts to adapt existing analytical procedures and design guidelines for the FRP-concrete interface to the SRP-concrete interface are still evolving. Double-lap direct shear tests on carbon FRP (CFRP)-concrete joints

and SRP-concrete joints revealed that the effective bond length of SRP is longer than that of CFRP (Triantafillou and Deskovic 1991). Single-lap direct shear test results of SRP-concrete joints reported in (Ascione et al. 2017) showed that: (i) different surface preparations influenced the bond behavior, (ii) higher density fiber sheets (i.e., smaller cord spacings) are not necessarily more effective than lower density fiber sheets since the interfacial capacity is mainly limited by the concrete substrate, and (iii) existing semi-empirical expressions developed to predict P_{deb} and L_e for FRP-concrete systems could potentially be used for SRP. Single-lap shear tests reported in (Carloni et al. 2017) showed that the bond behavior of SRP composites was similar to that of FRP composites, and that the fracture energy of SRP-concrete joints was independent of the fiber sheet density, whereas the effective bond length depends on the fiber sheet density. The conflicting results described above suggest that more data are needed to understand the bond behavior of SRP-concrete joints. Additionally, the behavior of SRP-concrete joints with relatively short bonded length (less than 120 mm) has not been heavily investigated.

This study aimed to explore the bond behavior of SRP-concrete joints tested in direct shear. This paper presents the results of an experimental campaign in which different test parameters, including composite bonded length and cord sheet density, were considered. The experimental results were used to determine the bond-slip relationship of the SRP-concrete interface and to predict the full-range load response. To consider a larger dataset, a database of SRP-concrete joint tests was established in which the test results from this study were supplemented with results of tests reported in the literature. Analytical equations derived to predict P_{deb} and L_e for FRP-concrete joints were examined to determine whether they can be applied to SRP-concrete joints.

2 Materials
2.1 Concrete
The concrete was produced from normal-weight dolomitic limestone coarse aggregate with a maximum size of 16 mm, natural river sand, and commercial Portland Type I/II cement. The concrete mixture had a design compressive strength of 30 MPa to represent concrete used in existing civil structures in need of strengthening. The mixture proportions by weight ratio were (cement: sand: aggregate)=(1:00: 3.33: 2.51), and the water-cement ratio was 0.59. The concrete compressive and splitting tensile strengths were obtained experimentally using 101.6 mm diameter × 203.2 mm long cylinders in accordance with ASTM C39/C39M (ASTM C39/C39M-17b 2017) and ASTM C496/C496M (ASTM C496, C496M 2017), respectively. The compressive and splitting

tensile strengths, each determined as the average of three tests, were 25.79 MPa (CoV = 0.08) and 2.47 MPa (CoV = 0.07), respectively.

2.2 Matrix

The polymeric matrix used in the SRP composite was a thixotropic epoxy (Kerakoll 2020). The tensile strength, shear strength, flexural elastic modulus, and secant Young's modulus under compression, according to the manufacturer (Kerakoll 2020), were > 14 MPa, > 20 MPa, > 2.5 GPa, and > 5.3 GPa, respectively.

2.3 Steel fibers

The SRP composite fibers were made of unidirectional high strength steel cords, see Fig. 1. Each cord had a cross sectional area (A_{cord}) of 0.538 mm^2 and consisted of five wires. Three straight wires formed the core of the cord, and two wires were twisted around them in a helical manner, see Fig. 1. The wires were galvanized with a zinc coating and were laid on a fiberglass mesh backing to facilitate installation. According to the manufacturer

(Kerakoll 2020), the fiber sheet had a tensile strength of > 3000 MPa, and an elastic modulus of > 190 GPa.

Different fiber sheet densities, defined in terms of net fiber weight per unit fiber sheet area (in g/m^2), were achieved by different cord spacings. Two fiber sheet densities were tested in this study, referred to herein as medium density (MD) and low density (LD) fibers, see Fig. 1a. Most tests in this study were conducted using the MD fibers because the direct shear test specimens with MD fibers achieved the desired failure mode (composite debonding), whereas the specimens with LD fibers failed due to fiber rupture, as discussed in Sect. 4. The properties of the fiber sheets provided by the manufacturer are listed in Table 1. It should be noted that the properties given in Table 1 generally apply to composites of relatively wide width, with a large number of cords.

Three MD bare fiber tensile coupons with 15 steel cords were tested in uniaxial tension, see Table 2. Figure 1b shows the tensile test of a MD bare fiber sheet. An extensometer was used to measure the axial strain in the fibers. The applied load-axial strain relationship of specimen BF_2 is plotted in Fig. 2. As the load approached the maximum load, one fiber chord ruptured followed
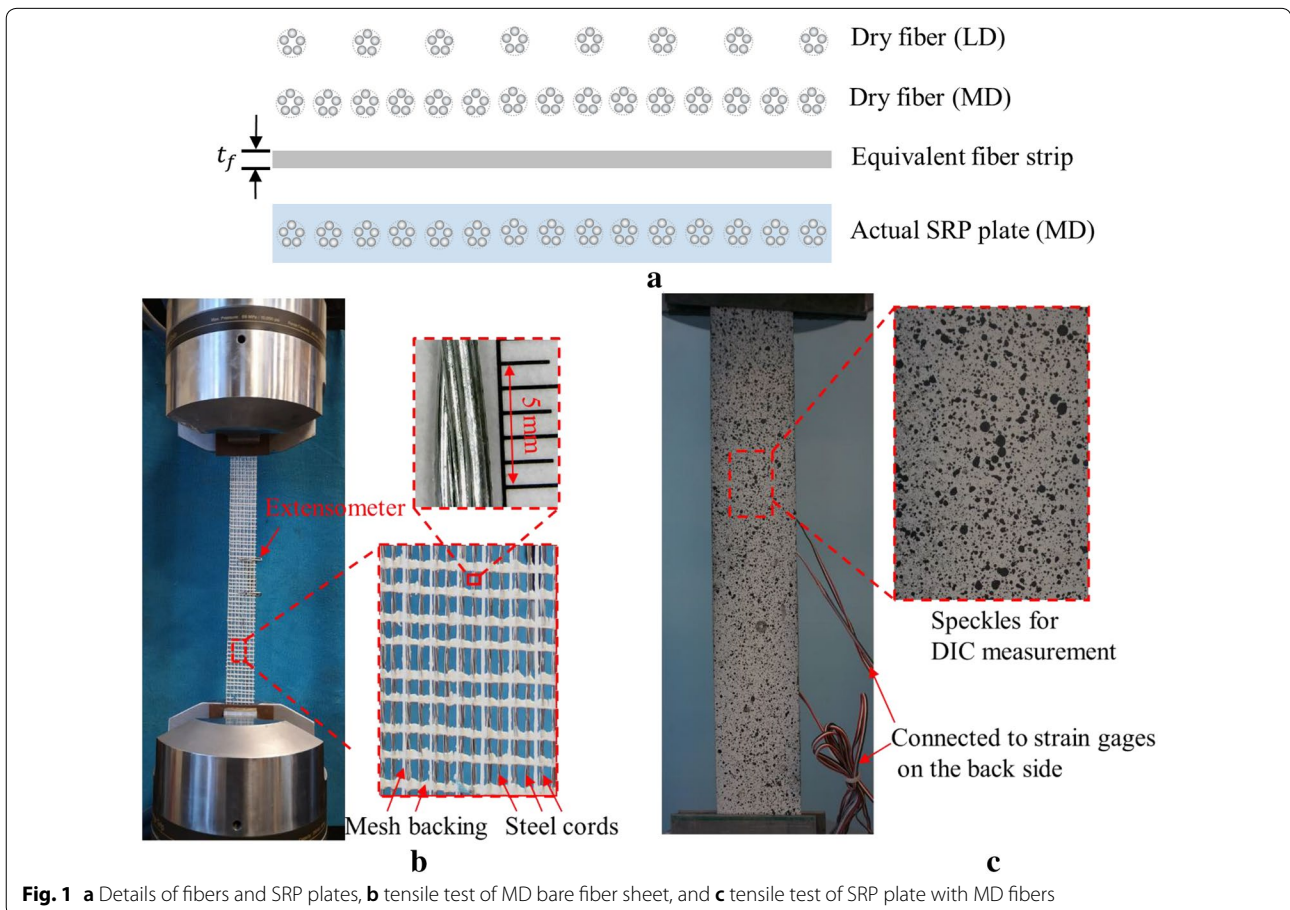

Fig. 1 **a** Details of fibers and SRP plates, **b** tensile test of MD bare fiber sheet, and **c** tensile test of SRP plate with MD fibers

Table 1 Properties of fibers provided by the manufacturer (Kerakoll 2020)

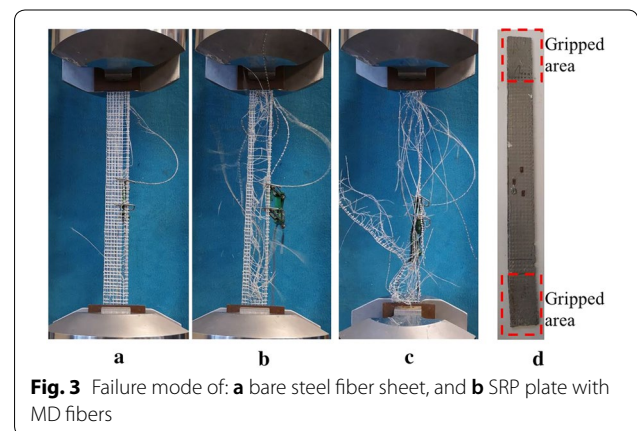| Fiber sheet type	Density of fiber sheets (g/m²)	Number of cords (/mm)	Equivalent thickness t_f (mm)	Break deformation (%)	Tensile strength (MPa)
Low density (LD)	600	0.157	0.084	>2	>3000
Medium density (MD)	1200	0.314	0.169	>2	>3000

Table 2 Tensile test results of bare steel wire sheet and SRP plate with MD fibers

Coupon ID	Type	Strain at 5 kN (10^{-6})	Elastic modulus (GPa)		Failure mode	Ultimate load (kN)
				Avg [CoV]		
BF_1	Bare MD fibers	3091	200.4	190.8 [0.05]	Gripped end fracture	16.24
BF_2	Bare MD fibers	3285	188.6		Gripped end fracture	17.33
BF_3	Bare MD fibers	3380	183.3		Fiber rupture	23.89
SRP_1	SRP with MD fibers	2548	232.3	257.2 [0.08]	Gripped end fracture	16.95
SRP_2	SRP with MD fibers	2299	257.3		Fiber rupture	21.73
SRP_3	SRP with MD fibers	2107	280.8		Gripped end fracture	17.01
SRP_4_D	SRP with MD fibers	2292	258.2		Fiber rupture	21.47
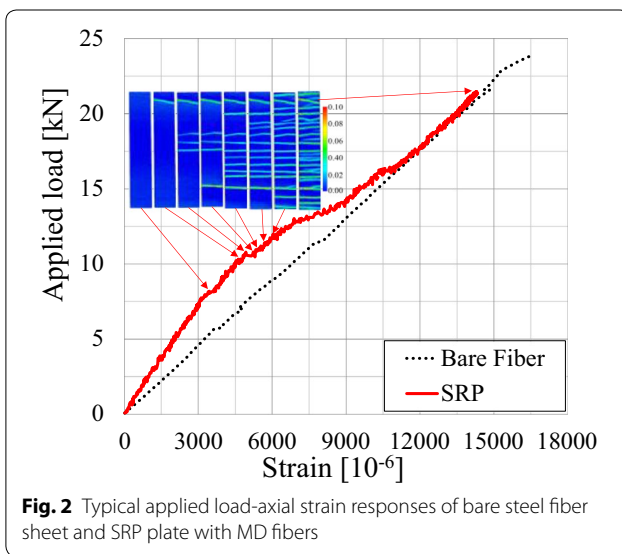
Fig. 2 Typical applied load-axial strain responses of bare steel fiber sheet and SRP plate with MD fibers

Fig. 3 Failure mode of: **a** bare steel fiber sheet, and **b** SRP plate with MD fibers

by sudden rupture of the remaining fiber chords, see Fig. 3b and c. The maximum applied load was 23.88 kN. Considering the actual cross sectional area of the fibers in the tensile coupon, 15×0.538 mm² $= 8.07$ mm², a maximum stress of 2959 MPa was obtained from the maximum load, which is similar to the value provided by the manufacturer. Based on the actual cross sectional area, the elastic modulus was determined from the secant slope at 5 kN, and values are reported in Table 2. The average elastic modulus for the MD bare fiber sheet was 190.8 GPa (CoV = 0.05). This value is slightly larger

(approximately 5%) than the values reported in (Ascione et al. 2017), where the cross sectional area of the fiber sheet was computed by multiplying the equivalent thickness of the fibers by the width of the assumed equivalent strip instead of using the area corresponding to the actual number of cords.

2.4 SRP plate

Four 50 mm wide × 4 mm thick SRP tensile coupons consisting of MD fiber sheets with 15 steel cords embedded in the polymeric matrix were fabricated and tested in tension, see Fig. 1a and b. Digital image correlation (DIC) (GOM 2020; Zhu et al. 2014) was employed on one of the four coupons to determine the axial strain along the fiber direction on the surface of the SRP plate. The images

were taken by a Sonyα6000 camera remotely controlled by a computer. With the control unit, the camera was triggered at a selected frequency. The images were evaluated using a commercial software package (GOM 2020).

The applied load-axial strain response of specimen SRP_4_D is plotted together with the DIC results of axial strain at different load levels in Fig. 2. Figure 2 shows that the stress–strain behavior is nonlinear. It can be seen that at the beginning of loading, the applied load increased linearly, and no cracks were observed on the SRP surface according to the DIC results. At a load level of approximately 12 kN, the first crack, marked by larger axial strain on the surface of the specimen shown in the DIC results, occurred within the SRP matrix along the transversal direction (perpendicular to the fibers), resulting in a reduction of the slope of the applied load-axial strain curve. With further increase in load, more cracks were observed on the surface of the SRP, and the existing cracks became wider. At the peak load, the average spacing of cracks was around 10 mm, see the multiple large axial strain bands in the DIC results.

Similar to the bare fiber test in Sect. 2.3, the secant slope at 5 kN was taken as the elastic modulus of the SRP plate, $E_{f,SRP}$, see Table 2. It should be noted that $E_{f,SRP}$ was determined with respect to the equivalent thickness of the fibers (t_f, see Table 1) for comparison with values reported in previous studies (Carloni et al. 2017; Santandrea 2018) and for use in calculations later in this paper. The average $E_{f,SRP}$ for the SRP tensile coupons with MD fibers was 257.2 GPa (CoV = 0.08). This value is similar to the values determined by similar tension tests of SRP plates with the same fibers but different sheet densities and polymer matrix reported in (Carloni et al. 2017; Santandrea 2018).

3 Methods
The bond behavior of SRP-concrete joints was studied experimentally using a single-lap direct shear test, which is commonly used to study the interfacial properties of fiber reinforced composites bonded to concrete. The test specimen consisted of a concrete prism and a SRP strip bonded to the concrete surface. The concrete prisms were 125 mm wide × 125 mm deep × 375 mm long. After casting the concrete, all concrete prisms and cylinders were cured under a plastic sheet for 24 h before being removed from the forms. After the removal of the forms, the prisms and cylinders were placed in the laboratory for curing. During the curing of specimens, the room temperature was approximately 15 ℃.

The concrete blocks were sandblasted prior to the application of the SRP strip. Only the longitudinal side faces cast directly against the formwork were used to bond the SRP strip, as suggested in (Carloni et al. 2017).

2 mm thick tape was used as formwork to control the location and dimensions of the SRP strip. A layer of matrix was applied to the surface, followed by the steel fiber strip. Then a second layer of tape was applied onto the first layer, and another coating layer of matrix was applied. The resulting thickness of the SRP strip was nominally 4 mm.

The concrete prism was mounted onto the base of a servo-hydraulic testing machine using a steel frame, see Fig. 4. Prior to mounting the specimen, steel plates were attached to the end of the SRP strip using a thermosetting epoxy and bolts in each corner of the steel plates, see Fig. 4. The bolts were tightened to allow for better gripping during testing and to reduce the likelihood of the fibers or SRP plate from slipping between the steel plates during testing. Two brackets were mounted onto the surface of the concrete specimen to hold two linear variable displacement transducers (LVDTs) during the test procedure. A Ω-shaped, cold-formed steel plate was affixed to the SRP strip right at the loaded end of the bonded area, see Fig. 4. The Ω-plate was used as a reaction surface for the LVDTs. The load was applied via displacement control where the value of displacement used to control the test was the average reading of the two LVDTs. The average reading of the two LVDTs was assumed to correspond to the slip at the loaded end, termed the global slip (*g*), of the SRP composite strip relative to the concrete substrate at the composite
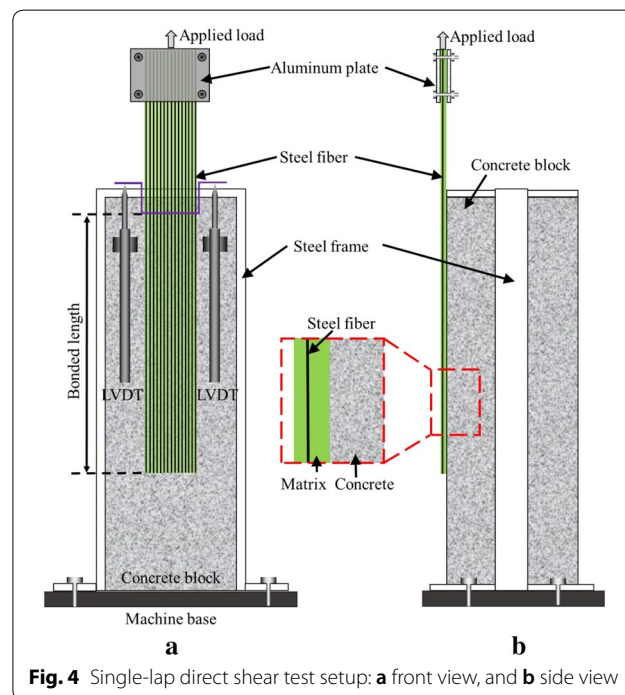

Fig. 4 Single-lap direct shear test setup: **a** front view, and **b** side view

loaded end. The load was applied via displacement control at a rate of 0.00084 mm/s, which is consistent with previous research (Carloni et al. 2017).

A total of 63 single-lap shear test specimens were included. The specimens were designated with the following convention: XD_L_i_(D or B), in which "XD" denotes the fiber sheet density see Table 1, "L" indicates the composite bonded length (in mm), "i" denotes the specimen number within the same series, "D", where present, denotes that DIC was used, and "B", where present, indicates that the fibers were bare outside the bonded area. All specimens are listed in Table 3.

4 Experimental results and discussion
In this section, the experimental load responses obtained from the single-lap shear tests described in Sect. 3 are presented.

4.1 Failure mode and general observations
The failure mode of each specimen is reported in Table 3. Regarding specimens with MD fibers, most specimens failed due to debonding of the composite, which occurred within the concrete adjacent to the matrix-concrete interface. A thin layer of concrete was still attached to the SRP strip after debonding failure (Fig. 5). The failure was brittle and catastrophic. Two specimens, MD_120_8 and MD_210_7_D, failed due to fiber rupture, with a maximum load of 22.70 kN and 24.12 kN, respectively. The maximum loads achieved by these specimens were the highest of all specimens and were approximately equal to the tensile strength of the fibers and SRP plate, see Table 2. All specimens with LD fibers failed due to fiber rupture, see Table 3.

From the beginning of loading to the failure of specimens, no obvious cracks were observed on the surface of the concrete substrate, nor were any cracking sounds noted. However, one salient difference between SRP- and FRP-concrete joints is that the SRP strips exhibited multiple cracks along the transversal direction, similar to the response of the SRP tensile coupons discussed in Sect. 2.4. As an example, Fig. 6 shows the load response of specimen MD_210_8_D and the axial strain along fiber direction measured by DIC. At Point A, initial cracking occurred at the loaded end of the specimen. After the applied load reached a peak value, see Point C in Fig. 6a, there was a dramatic load drop. The load drop was caused by the first wave of local debonding of a portion of the SRP strip near the loaded end, see the comparison between Points C and D in Fig. 6b. Then, with the increase of global slip, the transversal cracks became wider until the load reached another local peak, Point F, see Fig. 6a. After Point F, there was another dramatic load drop, which was caused by the formation of

another transversal crack, and the second wave of interfacial debonding, see the comparison between Points F, G, H, and I in Fig. 6b. Then the load increased to Point K and axial strain was recorded at the free end of the bonded area. The load increased again until the failure of the specimen, Point M, see Fig. 6a. At Point M, several large transversal cracks were detected by DIC along most of the bonded length, see Fig. 6b. The transversal cracks were slightly unsymmetrical, which is likely the result of non-uniform bonding conditions due to local variations in the concrete surface (e.g., presence of aggregate) since the load-history responses of the two LVDTs used to measure and control the loaded end slip were consistent with one another. The DIC results clearly show the initiation and widening of the transversal cracks caused by longitudinal interfacial cracking, which was visibly observed on the side of the specimen. The longitudinal interfacial crack formed at the loaded end and propagated towards the free end with the increasing global slip.

After failure of the specimens, in general, a relatively large piece of concrete detached from the substrate near the composite loaded end, while a smaller piece of concrete sometimes detached near the free end of the SRP strip (Fig. 5). The thickness of the concrete layer attached to the debonded SRP strip elsewhere varied approximately between 1 and 8 mm. The surface of the failure zone of the concrete prism was uneven, with the aggregate being clearly visible (Fig. 5).

4.2 Load responses and key values of load and global slip
The load responses of the single-lap shear tests are plotted in Figs. 7, 8, and 9 for all specimens, maintaining the distinction between different bonded lengths, fiber sheet densities, and presence/absence of the matrix in the unbonded region. Figure 7a and b show that, for specimens with a relatively short bonded length ($L = 30$ and 60 mm), the load increased almost linearly until failure. There was a consistent initial slope among different specimens. It is interesting to see the formation of a concrete bulb of thickness of 4–10 mm at the composite loaded end, see Fig. 5a and b. For specimens with a bonded length equal to or larger than 90 mm, Fig. 7c–h show that the initial linear response was followed by a non-linear branch until a larger load was achieved, which sometimes corresponded to the peak (maximum) load of the specimen. The drop in load that followed marks the onset of the interfacial crack propagation (Carloni et al. 2017), as explained in Sect. 4.1. For specimens with $L > 120$ mm, as the interfacial crack propagated, the load remained approximately constant with fluctuations until the failure of the specimen.

Figure 8 shows the load responses of the specimens with LD fibers and a bonded length $L = 240$ mm. It can

Table 3 Direct shear test results

Specimen ID	Failure mode	P_{max} (kN)	Avg [CoV]	g_{max} (mm)	g_{ult} (mm)	Avg [CoV]
MD_30_1	Debonding	7.95	6.80 [0.151]	0.271	0.298	0.190 [0.311]
MD_30_2	Debonding	5.08		0.111	0.128	
MD_30_3	Debonding	7.64		0.188	0.188	
MD_30_4	Debonding	6.63		0.147	0.155	
MD_30_5	Debonding	6.42		0.195	0.199	
MD_30_6	Debonding	7.10		0.160	0.169	
MD_60_1	Debonding	14.58	12.73 [0.106]	0.493	0.493	0.426 [0.168]
MD_60_2	Debonding	13.40		0.297	0.297	
MD_60_3	Debonding	10.56		0.402	0.402	
MD_60_4	Debonding	12.26		0.377	0.380	
MD_60_5	Debonding	13.47		0.458	0.461	
MD_60_6	Debonding	13.25		0.453	0.454	
MD_60_7	Debonding	11.62		0.493	0.496	
MD_90_1	Debonding	11.56	14.54 [0.177]	0.452	0.466	0.534 [0.247]
MD_90_2	Debonding	12.34		0.420	0.434	
MD_90_3	Debonding	12.90		0.498	0.508	
MD_90_4	Debonding	15.63		0.752	0.752	
MD_90_5	Debonding	16.23		0.641	0.690	
MD_90_6	Debonding	18.10		0.461	0.470	
MD_90_7_D	Debonding	15.03		0.284	0.418	
MD_120_1	Debonding	14.14	15.89 [0.098]	0.864	0.889	0.827 [0.083]
MD_120_2	Debonding	14.02		0.646	0.727	
MD_120_3	Debonding	14.44		0.707	0.895	
MD_120_4	Debonding	16.53		0.816	0.842	
MD_120_5	Debonding	16.27		0.741	0.743	
MD_120_6	Debonding	17.00		0.765	0.877	
MD_120_7	Debonding	18.39		0.771	0.771	
MD_120_8	Fiber rupture	22.70		1.365	1.365	
MD_120_9_D	Debonding	16.29		0.776	0.868	
MD_150_1	Debonding	16.00	15.40 [0.073]	0.715	0.807	0.840 [0.114]
MD_150_2	Debonding	14.84		0.659	0.866	
MD_150_3	Debonding	15.49		0.675	0.863	
MD_150_4	Debonding	16.47		0.651	1.001	
MD_150_5	Debonding	16.71		0.667	0.691	
MD_150_6	Debonding	13.44		0.556	0.873	
MD_150_7	Debonding	14.85		0.707	0.781	
MD_180_1	Debonding	14.85	16.29 [0.091]	1.197	1.216	0.966 [0.218]
MD_180_2	Debonding	16.38		0.611	0.611	
MD_180_3	Debonding	16.46		0.999	1.041	
MD_180_4	Debonding	14.52		0.890	0.895	
MD_180_5	Debonding	16.95		1.110	1.110	
MD_180_6_D	Debonding	18.59		0.919	0.921	

Table 3 (continued)

Specimen ID	Failure mode	P_{max} (kN)		g_{max} (mm)	g_{ult} (mm)	
			Avg [CoV]			Avg [CoV]
MD_210_1	Debonding	12.97	16.06 [0.117]	0.329	1.140	1.282 [0.179]
MD_210_2	Debonding	15.84		1.370	1.430	
MD_210_3	Debonding	14.85		1.109	1.133	
MD_210_4	Debonding	17.35		0.934	1.000	
MD_210_5	Debonding	15.40		1.699	1.699	
MD_210_6	Debonding	18.41		1.023	1.289	
MD_210_7_D	Fiber rupture	24.12		1.165	1.165	
MD_210_8_D	Debonding	17.59		0.189	1.285	
MD_240_1	Debonding	15.83	16.08 [0.133]	0.726	1.820	1.311 [0.321]
MD_240_2	Debonding	15.84		1.771	1.844	
MD_240_3	Debonding	17.98		0.842	0.842	
MD_240_4	Debonding	12.94		0.231	0.860	
MD_240_5	Debonding	13.73		1.081	1.510	
MD_240_6	Debonding	18.17		1.208	1.209	
MD_240_7_D	Debonding	18.10		0.941	1.094	
LD_240_1_D	Fiber rupture	13.36	12.11 [0.103]	0.341	0.341	0.412 [0.153]
LD_240_2_D	Fiber rupture	12.09		0.461	0.463	
LD_240_3_D	Fiber rupture	10.87		0.432	0.432	
MD_240_1_B	Debonding	13.86	17.32 [0.204]	0.221	1.794	1.219 [0.481]
MD_240_2_B	Debonding	17.19		0.562	1.241	
MD_240_3_B	Debonding	20.91		0.621	0.622	

be seen that the load response was initially linear with a slight softening behavior until around 12 kN where fiber rupture occurred, which provides a lower shear capacity of the SRP-concrete joints compared with specimens with MD fibers with the same bonded length.

Figure 9 shows the load responses of the specimens with MD fibers, bonded length $L = 240$ mm, and bare fibers in the unbonded region. Comparing the results with those in Fig. 7h, it can be seen that the load response is almost the same as the response of similar specimens with matrix along the unbonded region. This indicates that the presence of the matrix in the unbonded region did not significantly influence the results.

Values of the peak load, P_{max}, and the global slip at failure (referred to as the ultimate global slip), g_{ult}, are listed in Table 3. It should be noted that only specimens with the failure mode of debonding are considered when computing average values in Table 3. Figure 10 plots the relationship between P_{max} and L for all specimens with MD fibers that failed due to debonding, with the exception of those with bare fibers in the unbonded region. The results in Fig. 10 show that P_{max} increases as L increases from 30 mm to 120 mm, and then P_{max} remains nearly

constant for larger values of L. These results are used in Sect. 5 to determine the bond-slip relationship for the SRP-concrete interface.

Figure 11 plots the relationship between g_{ult} and L for specimens with MD fibers that failed due to debonding, with the exception of those with bare fibers in the unbonded region. The results in Fig. 11 show that g_{ult} increases with L, however, a large scatter was observed, especially for specimens with long bonded length.

5 Determination of bond–slip relationship from the peak load-bonded length relationship

It is generally assumed that composite-concrete debonding propagation can be idealized as a Mode-II fracture problem. A fictitious interface material is usually considered with zero thickness and a well-defined constitutive response (Lopez et al. 2007; Casadei et al. 2005; Chen and Teng 2001; Lu et al. 2005; Zhou et al. 2010). A relationship between interface shear stress (τ) and the relative slip (s) between the composite and concrete can be used to characterize the interface material. The interfacial bond stress-slip model developed by Dai et al. (Dai
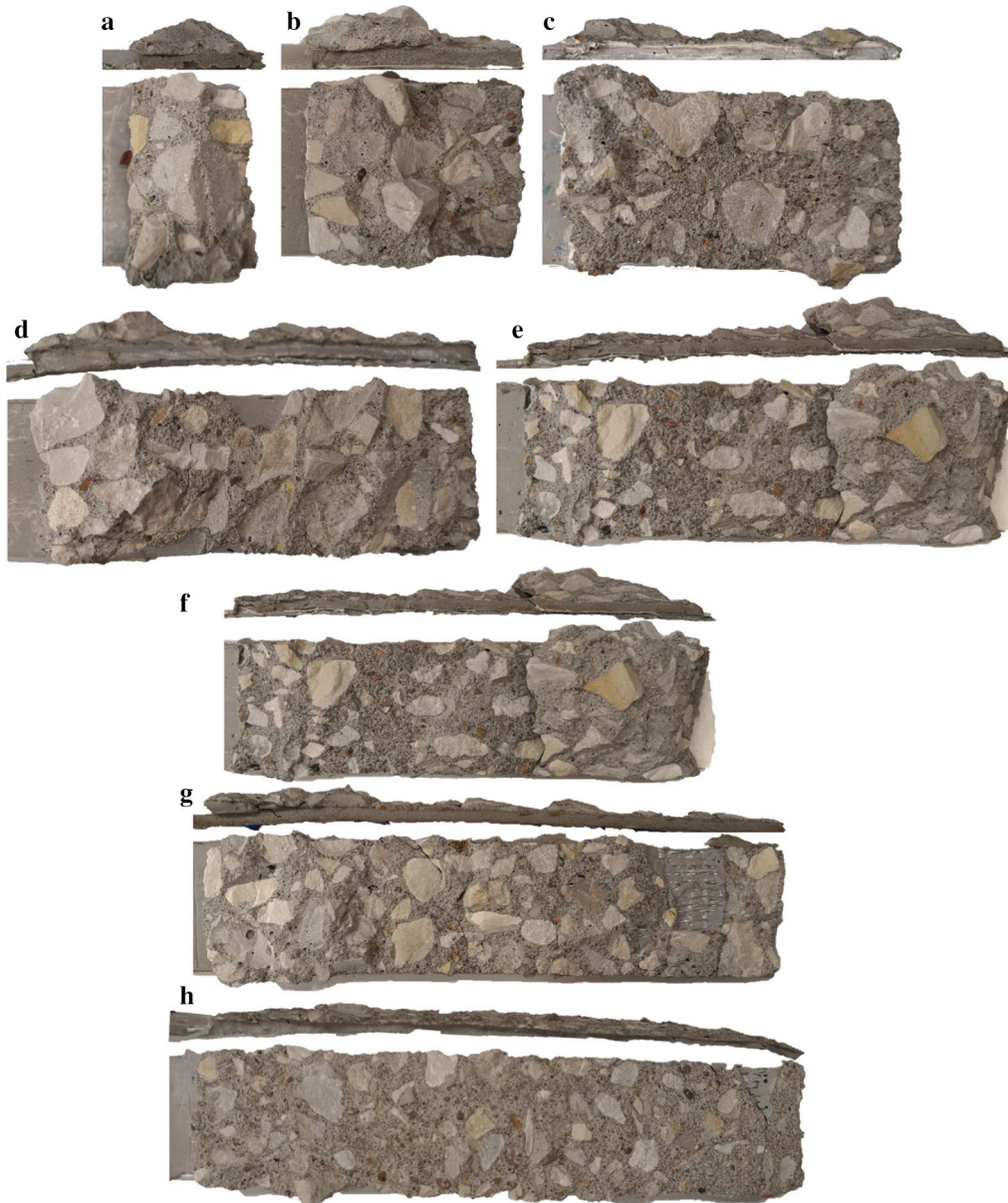
Fig. 5 Typical failure mode of single-lap shear test specimens with MD fibers and bonded length of: **a** 30 mm, **b** 60 mm, **c** 90 mm, **d** 120 mm, **e** 150 mm, **f** 180 mm, **g** 210 mm, and **h** 240 mm

et al. 2005), which has been widely used to characterize the FRP-concrete interface material, is:

$$\tau(s) = E_f t_f A^2 B\left(e^{-Bs} - e^{-2Bs}\right) \tag{1}$$

where $\tau(s)$ denotes the function of the bond-slip relationship, and E_f and t_f are the modulus of elasticity of the FRP and thickness of the fibers, respectively. A and B are parameters that define the peak value of shear stress and the shape of the $\tau(s)$ curve, which can be given as:

$$A = \sqrt{\frac{2G_f}{E_f t_f}} = 2.4\sqrt{\frac{\tau_m s_m}{E_f t_f}} \tag{2}$$

$$B = 0.693/s_m \tag{3}$$

where G_f is the interfacial fracture energy, representing the area under the $\tau(s)$ curve, which is related to P_{max} through the interface and is independent of the shape of the bond-slip curve (Dai et al. 2005). τ_m and s_m are
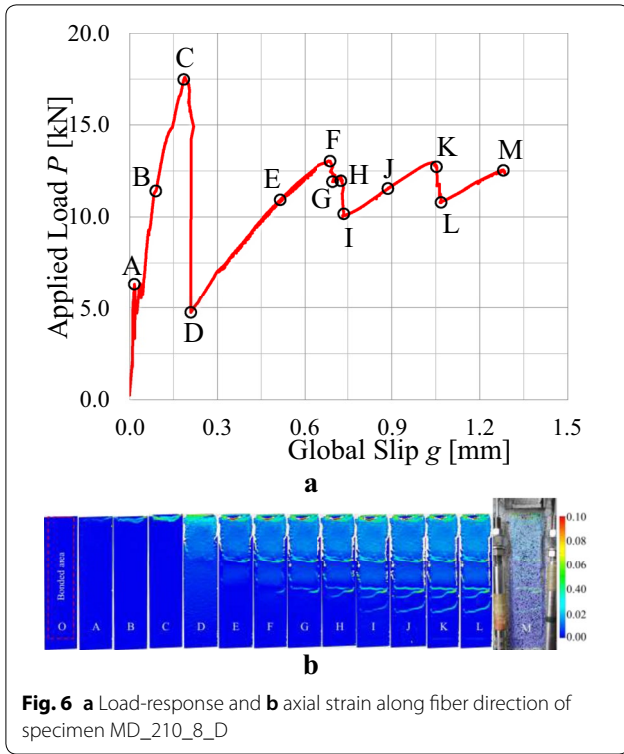
Fig. 6 a Load-response and **b** axial strain along fiber direction of specimen MD_210_8_D

the maximum shear stress and the corresponding slip, respectively.

An analytical solution of the full-range load response of specimens with infinite bonded length has been derived in (Dai et al. 2005). However, this solution adopted the assumption that the slip at free end, s_F, is zero, so it is not suitable for specimens with relatively short bonded lengths, since for short bonded lengths $s_F \neq 0$ (Liu and Wu 2012). Another solution that is suitable for all bonded lengths has been given by Liu and Wu (Liu and Wu 2012), in which the solution is driven by monotonically increasing s_F:

$$s(y) = \frac{1}{B}\ln\left[\frac{\eta\cosh\left(AB\sqrt{1-\eta^2}y\right)+1}{1-\eta^2}\right] \qquad (4)$$

$$\varepsilon(y) = A\frac{\eta\left(1-\eta^2\right)\sinh\left(AB\sqrt{1-\eta^2}y\right)}{1+\eta\cosh\left(AB\sqrt{1-\eta^2}y\right)} \qquad (5)$$

$$\tau(y) = E_f t_f A^2 B\eta\left(1-\eta^2\right)\frac{\eta+\cosh\left(AB\sqrt{1-\eta^2}y\right)}{\left[1+\eta\cosh\left(AB\sqrt{1-\eta^2}y\right)\right]^2} \qquad (6)$$

where $s(y)$, $\varepsilon(y)$, and $\tau(y)$ are the slip, axial strain, and shear stress along the bonded length of the FRP,

respectively. The term η is used to simplify the form of the equations and is given by $\eta = 1 - e^{-Bs_F}$. The global slip (g) and applied load (P) are given as:

$$g = \frac{1}{B}\ln\left[\frac{\eta\cosh\left(AB\sqrt{1-\eta^2}L\right)+1}{1-\eta^2}\right] \qquad (7)$$

$$P = E_f t_f b_f A\frac{\eta\sqrt{1-\eta^2}\sinh\left(AB\sqrt{1-\eta^2}L\right)}{1+\eta\cosh\left(AB\sqrt{1-\eta^2}L\right)} \qquad (8)$$

An approximate relationship between P_{max} and L has been given in (Liu and Wu 2012) as:

$$P_{max} = AE_f t_f b_f \tanh(0.3ABL) \qquad (9)$$

Using the modulus $E_{f,SRP} = 257.2$ GPa determined in Sect. 2 of this paper and $t_f = 0.169$ mm (Table 1), the parameters of A and B were fitted with the experimental results in Fig. 10 by Eq. (9) for all MD fiber specimens that failed due to interfacial debonding excluding the specimens with bare fibers outside the bonded area. The results are $A = 0.00725$ mm/mm and $B = 7.58$/mm, with $R^2 = 0.996$, and the corresponding $\tau(s)$ determined by Eq. (1) is shown in Fig. 12. It should be noted that although there is large scatter of the experimental load response of specimens with the same bonded length, see Fig. 7, the fitting of P_{max} led to a high R^2 value. Solving Eqs. (2) and (3) gives $s_m = 0.0915$ mm and $\tau_m = 4.386$ MPa.

Substituting the fitted results of A and B into Eqs. (7) and (8), the full-range load response can be determined for each bonded length, and the results are shown in Fig. 7 by the curves labeled as "*Ana.*". It can be seen that the analytical load response matched well with the experimental load response of the corresponding specimens, even though there is larger scatter among different specimens with the same bonded length. It should be pointed out that an important difference between the analytical and experiments results is that there is no experimental (measured) response after the ultimate global slip (g_{ult}) is reached. The reason is that for specimens with relatively long bonded length, there is a snap-back phenomenon in the analytical P-g response, which is attributed to the drop in strain in the fibers close to loaded end (Liu and Wu 2012). Since the experimental tests in the present study were conducted by increasing the global (loaded end) slip, the applied load dropped dramatically when the snap-back phenomenon was about to occur, thereby terminating the loading process. Therefore, the snap-back phenomenon could not be captured experimentally using the control mode employed in this study, however the snap-back phenomenon has been observed in experiments of FRP-concrete joints that

Fig. 7 Loads responses of single-lap shear specimens with MD fibers and bonded length *L* = **a** 30 mm, **b** 60 mm, **c** 90 mm, **d** 120 mm (Note MD_120_8 not shown), **e** 150 mm, **f** 180 mm, **g** 210 mm (Note MD_210_7_D not shown), and **h** 240 mm. All specimens shown failed due to debonding of the composite

employed a different control mode (Carrara et al. 2011) and also in analytical work (Liu and Wu 2012). For bonded lengths less than a critical length (L_c), the snap-back phenomenon does not occur. L_c is given in (Liu and Wu 2012) as:

$$L_c = \frac{4.57}{AB} \tag{10}$$

Considering the values of *A* and *B* determined above, Eq. (10) gives $L_c = 83$ mm. For $L > L_c$, the ultimate global slip will occur after the peak load is reached, and the approximate solution of η is given by (Liu and Wu 2012):

$$\eta_c = \frac{\text{acoth}\left(\frac{ABL + 38.5}{42.8}\right)}{4.0} \tag{11}$$

For $L \leq L_c$ no snap-back occurs, and theoretically the experimental loading should capture the whole process including the post-peak behavior, similar to the results shown for fiber reinforced cementitious matrix (FRCM)-concrete joints in (Zou et al. 2020). However, for specimens with short bonded lengths, since the debonding process is brittle, the loading will usually terminate suddenly at the peak load, and the global slip at peak load will be taken as the ultimate slip. Figure 11 compares the analytical and experimental values of g_{ult} for the experimental bonded lengths considered. Two additional analytical bonded lengths were considered ($L = 70$ mm and 83 mm) corresponding to values equal to and slightly less than L_c as discussed above. It can be seen that the analytical g_{ult} is slightly lower than the experimental results for specimens with bonded length $L < 150$ mm, whereas it matched well with the experimental results for $L \geq 150$ mm.

Figure 10 shows that P_{max} approaches approximately 16 kN asymptotically as *L* increases. In engineering applications, the bond length corresponding to wP_{max}, where *w* is a value sufficiently close to but less than 1.0 (typically 0.96 or larger (Yuan et al. 2001; Yuan et al. 2004)), is estimated as the effective bond length L_e. L_e is given as (Liu and Wu 2012):

$$L_e = \frac{\text{atanh}(w)}{0.3AB} \tag{12}$$

Using the fitted results of *A* and *B* in this paper and $w = 0.96$, Eq. (12) gives $L_e = 6.48/(AB) = 118$ mm.

6 Evaluation of equations for FRP-concrete bond-slip behavior

Several authors have proposed equations to predict the maximum load P_{max} for FRP-concrete joints that fail due to debonding of the composite within the concrete substrate and the effective bond length L_e. This section evaluates the validity of four commonly-used equations to predict P_{max} and L_e for SRP-concrete joints.

6.1 Existing Equations

Chen and Teng proposed a semi-empirical equation to predict P_{max} and L_e based on a modification of an existing fracture mechanics model with suitable simplifications (Chen and Teng 2001). The equation is given as:

$$P_{max} = 0.427\beta_l\beta_w b_f L_e \sqrt{f_c'} \tag{13}$$

where, $\beta_w = \sqrt{\frac{2 - b_f/b_c}{1 + b_f/b_c}}$, and $\beta_l = \begin{cases} 1, & if \quad L \geq L_e \\ \sin\left(\frac{\pi L}{2L_e}\right), & if \quad L < L_e \end{cases}$.

The effective bond length L_e is given as:

$$L_e = \sqrt{\frac{E_f t_f}{\sqrt{f_c'}}} \tag{14}$$

Lu et al. proposed the following equation based on a meso-scale finite element analysis (Lu et al. 2005):

$$P_{max} = \beta_l b_f \sqrt{2E_f t_f G_f} \tag{15}$$

where $G_f = 0.308\beta_w^2\sqrt{f_t}$, $\beta_w = \sqrt{\frac{2.25 - b_f/b_c}{1.25 + b_f/b_c}}$,

$\beta_l = \begin{cases} 1, & if \quad L \geq L_e \\ \frac{L}{L_e}\left(2 - \frac{L}{L_e}\right), & if \quad L < L_e \end{cases}$ and f_t is the tensile

strength of concrete. L_e is given as:

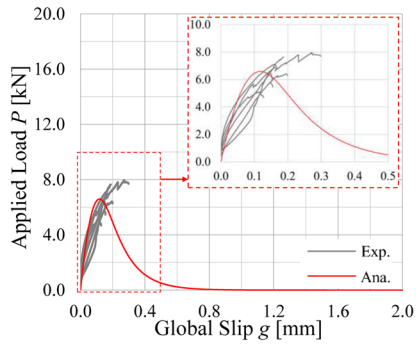$$L_e = 1.33\frac{E_f t_f}{f_t} \tag{16}$$
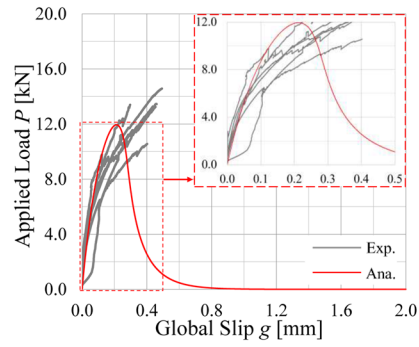
Units of MPa and mm shall be used in Eqs. (13)–(16).

Neubauer and Rostasy proposed the following equation (Neubauer and Rostasy 1997):

$$P_{max} = \begin{cases} 0.64\beta_w b_f \sqrt{E_f t_f f_t}, & if \quad L \geq L_e \\ 0.64\beta_w b_f \sqrt{E_f t_f f_t}\frac{L}{L_e}\left(2 - \frac{L}{L_e}\right), & if \quad L < L_e \end{cases} \tag{17}$$
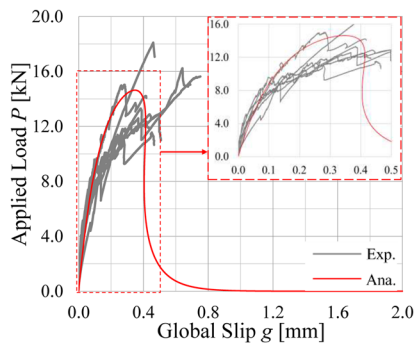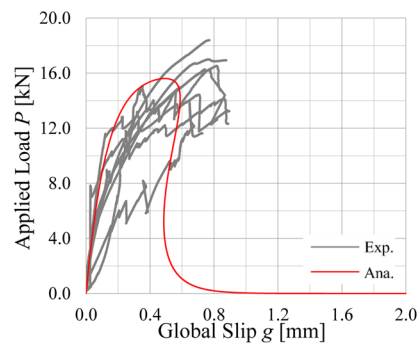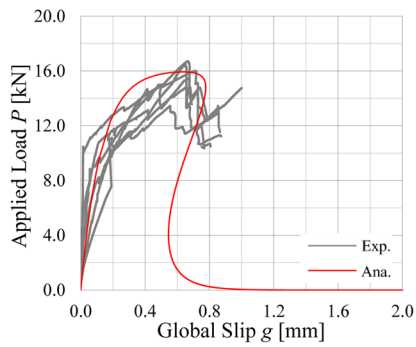
a

b

c

d

e

f

g

h

Fig. 8 Load responses of single-lap shear specimens with LD fibers and bonded length $L = 240$ mm. All specimens failed due to fiber rupture

Fig. 10 Peak load-bonded length relationship of specimens with MD fibers that failed due to debonding of the composite

Fig. 9 Load responses of single-lap shear specimens with MD fibers, bonded length $L = 240$ mm, and bare fibers outside the bonded area

Fig. 11 Ultimate global slip-bonded length relationship of specimens with MD fibers that failed due to debonding of the composite
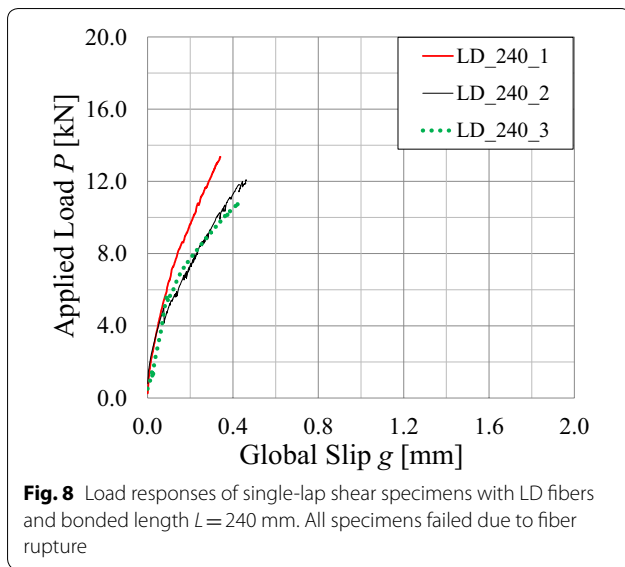
where $\beta_w = \sqrt{1.125 \frac{2 - b_f/b_c}{1 + b_f/400}}$, and L_e is given by:

$$L_e = \sqrt{\frac{E_f t_f}{2 f_t}} \tag{18}$$

Maeda et al. proposed the following equation (1997):

$$P_{max} = \begin{cases} \tau_u b_f L_e, & if \quad L \geq L_e \\ \tau_u b_f L, & if \quad L < L_e \end{cases} \tag{19}$$

where $\tau_u = 110.2 \times 10^{-6} E_f t_f$, and L_e is given by:

$$L_e = e^{6.13 - 0.580 \ln(10^{-3} E_f t_f)} \tag{20}$$

Units of MPa and mm shall be used in Eqs. (19) and (20).

The models described above have been calibrated based on experimental data. It should be noted the model by Maeda et al. (1997) is the only model considered herein that does not consider the effect of the concrete strength.

6.2 Comparison Between Experimental Maximum Load and Prediction by Existing Equations

In order to examine the validity of the equations described in Sect. 6.1 for SRP-concrete joints, a database of test results was collected from the literature (Ascione et al. 2017; Santandrea 2018). The database included the results of the present study as well as others that met the

Fig. 12 Bond-slip relationship for SRP-concrete joints with MD fibers determined from the experimental results
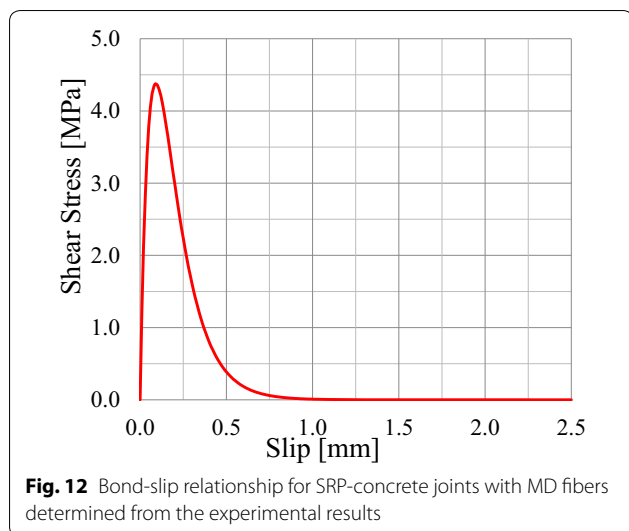
following criteria: (1) the specimen was tested in single-lap shear; (2) the specimen failed due to interfacial debonding; and (3) the elastic modulus of the SRP strip $E_{f,SRP}$ with the corresponding sheet density has been reported in the literature. In addition, specimens with a loading rate that was dramatically different from the rate utilized in this study (0.00084 mm/s) and in (Santandrea 2018) were excluded. The database included 170 test results and is presented in Additional file 1. Test specimens included SRP strips with three different sheet densities, and the SRP composite was provided by the same manufacturer. Values of $E_{f,SRP}$ were reported in Sect. 2.4 or in (Santandrea 2018). The compressive strength of concrete ranged from 12.8 to 39.7 MPa. For the specimens reported in 0, the tensile strength of concrete was not reported; therefore the expression $f_t' = 0.3f_c'^{2/3}$ from Eurocode 2 (Bamforth et al. 2008) was used to determine the concrete tensile strength of strength classes $\leq$ C50/60.

Figure 13 plots the predicted versus experimental value of P_{max} determined by Eqs. (13), (15), (17), and (19). The average ratio of P_{max} predicted by Eq. (13) to the corresponding experimental value is 0.95 with a CoV of 0.28. The average ratio of P_{max} predicted by Eq. (15) to the corresponding experimental value is 0.97 with a CoV of 0.29. The average ratio of P_{max} predicted by Eq. (17) to the corresponding experimental value is 1.16 with a CoV of 0.29. The average ratio of P_{max} predicted by Eq. (19) to the corresponding experimental value is 1.11 with a CoV of 0.32. Thus, all equations are in reasonable agreement with the experimental results, but Eqs. (13) and (15) tend to underestimate the experimental value of P_{max}, whereas Eqs. (17) and (19) tend to overestimate the experimental value of P_{max}. The variation is mainly caused by the large scatter of the test data of (Ascione et al. 2017), which can

be attributed, in part, to the fact that different surface treatments were evaluated in that study, which resulted in different strengths of the concrete adjacent to the bond adhesive. In addition, it should be noted that the elastic modulus $E_{f,SRP}$ considered in this evaluation corresponds to the initial response of the SRP plate tensile stress–strain behavior, as discussed in Sect. 2.4. Although the stress–strain response becomes non-linear at relatively high axial strain levels, (see Fig. 2), this simplification was justified by results in (Carloni et al. 2017) that show that the axial strain in the SRP strip along the bonded length reduces rapidly with increasing distance from the loaded end. However, future work should investigate the effect of the non-linear response of the SRP plate, which may help to improve the overall accuracy of the analyses and predicted results.

For the specimens with MD fibers that exhibited the failure mode of debonding in this study, the effective bond length L_e predicted by Eqs. (14), (16), (18), and (20) is 93 mm, 113 mm, 94 mm, and 51 mm, respectively. All four equations underestimated the effective bond length compared with the results given by Eq. (12) of 118 mm. Of the four equations, Eq. (16) has the best accuracy (within 4%).

7 Conclusions

This work presented the results of an experimental study carried out to determine the load-carrying capacity of SRP-concrete joints and the bond slip model based on experimental data acquired from single-lap direct shear test specimens. A database of SRP-concrete joint test results was established, and the results were used to examine the validity of equations developed for FRP-concrete joints to predict the maximum transferrable load and the effective bond length. Based on the findings of this study, the following conclusions are drawn:

1. Tension tests of SRP plates showed that the axial stress–strain behavior is nonlinear. These results are consistent with results reported in the literature for SRP plates with different sheet densities (Santandrea 2018).
2. Single-lap direct shear specimens with low density fibers tended to fail due to fiber rupture, whereas specimens with medium density fibers tended to fail in composite debonding. Debonding occurred due to fracture of the concrete within a thin layer beneath the SRP strip, similar to the behavior of FRP-concrete joints. These results suggest that fiber sheets with higher densities (smaller cord spacings) may not be more effective than those with lower densities since the interfacial capacity is limited by the properties of the substrate.
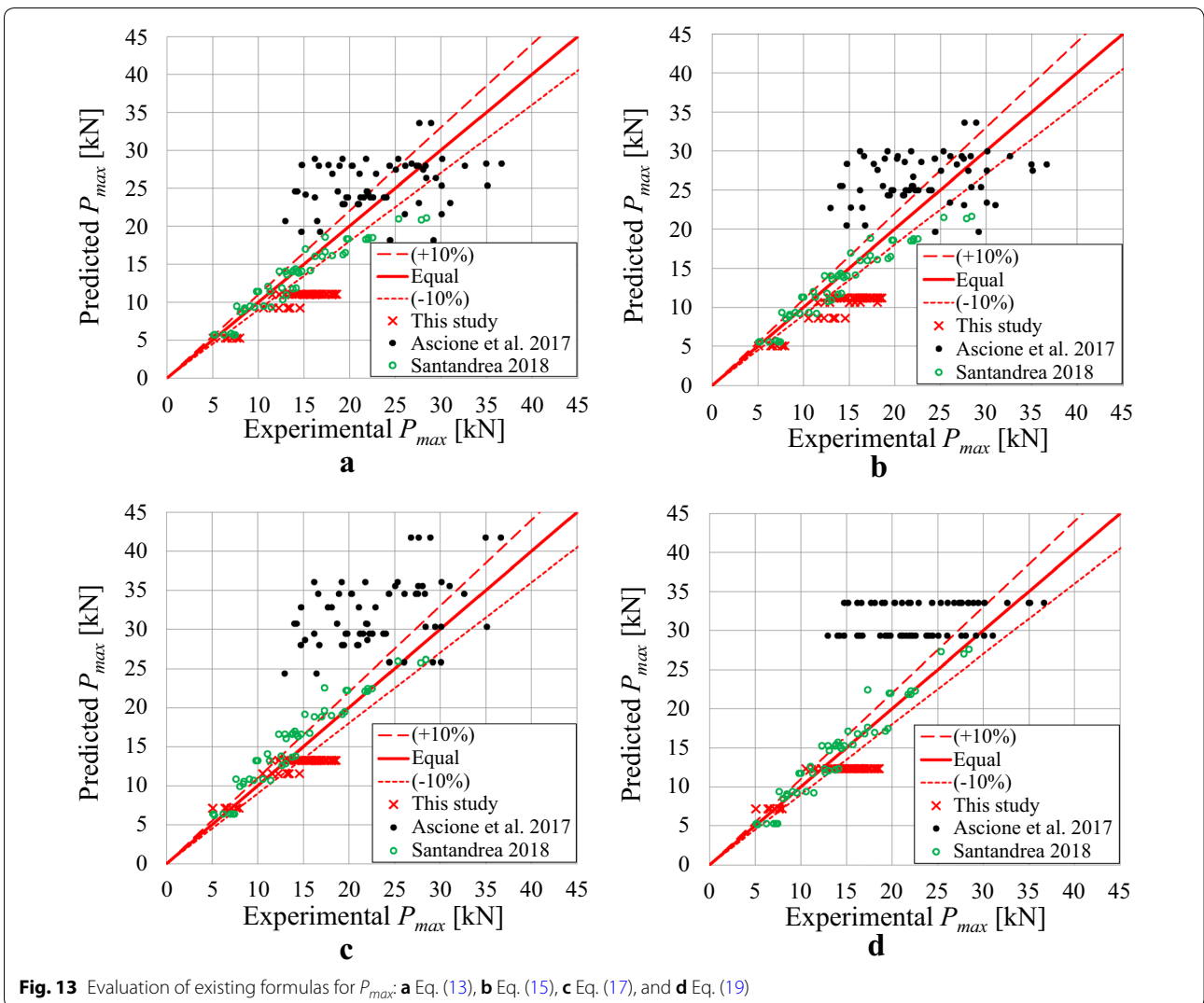
Fig. 13 Evaluation of existing formulas for P_{max}: **a** Eq. (13), **b** Eq. (15), **c** Eq. (17), and **d** Eq. (19)

3. The maximum load increased with the bonded length to a constant value. By fitting the maximum load-bonded length relationship, a nonlinear bond-slip relationship was obtained with a maximum shear stress of 4.386 MPa and a corresponding slip of 0.0915 mm. The analytical load response was in reasonable agreement with the experimental results.

4. The effective bond length is approximately 118 mm for specimens with medium density fibers.

5. A database of 170 SRP-concrete joints was established from the results of this study and supplemented with others collected from the literature. Existing equations proposed for FRP-concrete debonding behavior showed reasonable prediction of the maximum load with an average error less than 15%. However, future work should investigate the effect of the non-linear response of the SRP plate,

which may help to improve the overall accuracy of the analyses and predicted results.

6. The equations for FRP composites considered in this study underestimated the effective bonded length for the specimens with medium density fibers that failed in debonding.

Supplementary information

Additional file 1. SRP-concrete direct shear test database.

Authors' contributions

LHS supervised this project and the overall research such as the test plan, test results, and conclusions. She also suggested the test variables and reviewed the organization and language of this paper. XZ designed the testing program, carried out the experiments, analyzed the data, and wrote the first version of this paper. Both authors read and approved the final manuscript.

Authors' information

Xingxing Zou is a doctoral student in the Department of Civil, Architectural, and Environmental Engineering at Missouri University of Science and Technology. His research interests include the use of advanced composites for new structures and for strengthening and retrofitting existing concrete structures. He is also studying nondestructive evaluation of strengthened structures.

Lesley H. Sneed is an Associate Professor and the Stirrat Faculty Scholar in the Department of Civil, Architectural, and Environmental Engineering at Missouri University of Science and Technology. She has been actively involved in research and design of reinforced concrete structures with focus on the behavior of large-scale reinforced and prestressed concrete structural elements. Her current research interests include the shear and torsional behavior of concrete structures, repair and strengthening of structures subjected to seismic loading or other extreme hazards, and evaluation of existing structures.

Funding

Availability of data and materials

Not applicable.

Competing interests

The authors declare that they have no competing interests.

References

ACI 440.2R-17. (2017). *Guide for the Design and Construction of Externally Bonded FRP Systems for Strengthening Concrete Structures*. Farmington Hills: American Concrete Institute.

Alabdulhady, M. Y., & Sneed, L. H. (2019). Torsional strengthening of reinforced concrete beams with externally bonded composites: A state of the art review. *Construction and Building Materials, 205,* 148–163.

Ascione, F., Lamberti, M., Napoli, A., Razaqpur, G., & Realfonzo, R. (2017). An experimental investigation on the bond behavior of steel reinforced polymers on concrete substrate. *Composite Structures, 181,* 58–72.

ASTM C39/C39M-17b. (2017). Standard test method for compressive strength of cylindrical concrete specimens. West Conshohocken, Pam: ASTM International.

ASTM C496, C496M. (2017). *Standard Test Method for Splitting Tensile Strength of Cylindrical Concrete Specimens* (p. 2011). West Conshohocken: ASTM International.

Attari, N., Amziane, S., & Chemrouk, M. (2012). Flexural strengthening of concrete beams using CFRP, GFRP and hybrid FRP sheets. *Construction and Building Materials, 37,* 746–757.

Bakis, C. E., Bank, L. C., Brown, V., Cosenza, E., Davalos, J. F., Lesko, J. J., et al. (2002). Fiber-reinforced polymer composites for construction-State-of-the-art review. *Journal of composites for construction, 6*(2), 73–87.

Bamforth, P., Chisholm, D., Gibbs, J., & Harrison, T. (2008). Properties of concrete for use in Eurocode 2.

Carloni, C., Santandrea, M., & Imohamed, I. A. O. (2017). Determination of the interfacial properties of SRP strips bonded to concrete and comparison between single-lap and notched beam tests. *Engineering Fracture Mechanics, 186,* 80–104.

Carrara, P., Ferretti, D., Freddi, F., & Rosati, G. (2011). Shear tests of carbon fiber plates bonded to concrete with control of snap-back. *Engineering Fracture Mechanics, 78*(15), 2663–2678.

Casadei, P., Nanni, A., Alkhrdaji, T., & Thomas, J. (2005). Performance of double-T prestressed concrete beams strengthened with steel reinforcement polymer. *Advances in Structural Engineering, 8*(4), 427–442.

Chen, W., Pham, T. M., Sichembe, H., Chen, L., & Hao, H. (2018). Experimental study of flexural behaviour of RC beams strengthened by longitudinal and U-shaped basalt FRP sheet. *Composites Part B Engineering, 134,* 114–126.

Chen, J. F., & Teng, J. G. (2001). Anchorage strength models for FRP and steel plates bonded to concrete. *Journal of Structural Engineering, 127*(7), 784–791.

Dai, J., Ueda, T., & Sato, Y. (2005). Development of the nonlinear bond stress–slip model of fiber reinforced plastics sheet–concrete interfaces with a simple method. *Journal of composites for construction, 9*(1), 52–62.

Figeys, W., Schueremans, L., Brosens, K., & Van Gemert, D. (2005). Strengthening of concrete structures using steel wire reinforced polymer. *ACI Special Publication, 230,* 43.

Figeys, W., Schueremans, L., Van Gemert, D., & Brosens, K. (2008). A new composite for external reinforcement: Steel cord reinforced polymer. *Construction and Building Materials, 22*(9), 1929–1938.

GOM: https://www.gom.com/3d-software/gom-correlate-professional.html (Accessed Feb. 2020)

Górski, M., Krzywon, R., Dawczynski, S., & Greppi, R. (2013) Structural strengthenings based on SRP and SRG composites. International Conference on Engineering UBI, Nov 27-29, University of Beira Interior - Covilhã, Portugal.

Hii, A. K., & Al-Mahaidi, R. (2007). Torsional capacity of CFRP strengthened reinforced concrete beams. *Journal of Composites for Construction, 11*(1), 71–80.

Kerakoll S.p.A. http://www.kerakoll.com. Accessed Feb 2020.

Khalifa, A., & Nanni, A. (2000). Improving shear capacity of existing RC T-section beams using CFRP composites. *Cement & Concrete Composites, 22*(3), 165–174.

Kim, Y. J., Fam, A., Kong, A., & El-Hacha, R. (2005). Flexural strengthening of RC beams using steel reinforced polymer (SRP) composites. *ACI Special Publication, 230,* 93.

Liu, K., & Wu, Y. F. (2012). Analytical identification of bond–slip relationship of EB-FRP joints. *Composites Part B Engineering, 43*(4), 1955–1963.

Lopez, A., Galati, N., Alkhrdaji, T., & Nanni, A. (2007). Strengthening of a reinforced concrete bridge with externally bonded steel reinforced polymer (SRP). *Composites Part B Engineering, 38*(4), 429–436.

Lu, X. Z., Teng, J. G., Ye, L. P., & Jiang, J. J. (2005). Bond–slip models for FRP sheets/plates bonded to concrete. *Engineering Structures, 27*(6), 920–937.

Maeda, T., Asano, Y., Sato, Y., Ueda, T., & Kakuta, Y. (1997). "A study on bond mechanism of carbon fiber sheet." Non-Metallic (FRP) Reinforcement for Concrete Struct., In: Proc., 3rd Int. Symp., Japan Concrete Institute, Sapporo, 1, pp 279–285

Matana, M., Nanni, A., Dharani, L., Silva, P., & Tunis, G. (2005). Bond performance of steel reinforced polymer and steel reinforced grout. Proceedings of the International Symposium on Bond Behaviour of FRP in Structures, BBFS, 125–132).

Mitolidis, G. J., Salonikios, T. N., & Kappos, A. J. (2008). Mechanical and bond characteristics of SRP and CFRP reinforcement—A comparative research. *Open Construction and Building Technology Journal, 2,* 207–216.

Mukhtar, F. M., & Faysal, R. M. (2018). A review of test methods for studying the FRP-concrete interfacial bond behavior. *Construction and Building Materials, 169,* 877–887.

Neubauer, U., & Rostasy, F. S. (1997). Design aspects of concrete structures strengthened with externally bonded CFRP plates. In: Proc., 7th Int. Conf. on Struct. Faults and Repairs, ECS Publications, Edinburgh, Scotland, 2, 109–118.

Pan, J., & Leung, C. K. (2007). Debonding along the FRP–concrete interface under combined pulling/peeling effects. *Engineering Fracture Mechanics, 74*(1–2), 132–150.

Pecce, M., Ceroni, F., Prota, A., & Manfredi, G. (2006). Response prediction of RC beams externally bonded with steel-reinforced polymers. *Journal of Composites for Construction, 10*(3), 195–203.

Prota, A., Manfredi, G., Nanni, A., Cosenza, E., & Pecce, M. (2004). Flexural strengthening of RC beams using emerging materials: Ultimate behavior. Proceedings of 2nd International Conference on FRP Composites in Civil Engineering, CICE 2004, Adelaide, Australia, 2004, 163–170.

Santandrea, M. (2018). Bond behavior between fiber reinforced composites and quasi-brittle material interfaces. Dissertation. University of Bologna.

Triantafillou, T. C., & Deskovic, N. (1991). Innovative prestressing with FRP sheets: mechanics of short-term behavior. *Journal of Engineering Mechanics, 117*(7), 1652–1672.

Wobbe, E., Silva, P., Barton, B. L., Dharani, L. R., Birman, V., Nanni, A., & Tunis, G. (2004). Flexural Capacities of RC Beams Externally Bonded with SRP and SRG. http://www.hardwirellc.com/Downloads/Flex_Capacity.pdf, 2004, 8 pp.

Wu, Y. F., & Jiang, C. (2013). Quantification of bond-slip relationship for externally bonded FRP-to-concrete joints. *Journal of Composites for Construction, 17*(5), 673–686.

Yuan, H., Teng, J. G., Seracino, R., Wu, Z. S., & Yao, J. (2004). Full-range behavior of FRP-to-concrete bonded joints. *Engineering Structures, 26*(5), 553–565.

Yuan, H., Wu, Z., & Yoshizawa, H. (2001). Theoretical solutions on interfacial stress transfer of externally bonded steel/composite laminates. *Doboku Gakkai Ronbunshu, 2001*(675), 27–39.

Zhang, D., Gu, X., Yu, Q., Huang, H., Wan, B., & Jiang, C. (2018). Fully probabilistic analysis of FRP-to-concrete bonded joints considering model uncertainty. *Composite Structures, 185,* 786–806.

Zhou, Y. W., Wu, Y. F., & Yun, Y. (2010). Analytical modeling of the bond–slip relationship at FRP-concrete interfaces for adhesively-bonded joints. *Composites Part B Engineering, 41*(6), 423–433.

Zhu, H., Wu, G., Shi, J., Liu, C., & He, X. (2014). Digital image correlation measurement of the bond–slip relationship between fiber-reinforced polymer sheets and concrete substrate. *Journal of Reinforced Plastics and Composites, 33*(17), 1590–1603.

Zou, X., Sneed, L. H., & D'Antino, T. (2020). Full-range behavior of fiber reinforced cementitious matrix (FRCM)-concrete joints using a trilinear bond-slip relationship. Composite Structures, 112024.

Publisher's Note